Fast and Noninvasive Fluorescence Imaging of Biological Tissues *In Vivo* Using a Flying-Spot Scanner

Nirmala Ramanujam*, JinXian Chen, Kirk Gossage, Rebecca Richards-Kortum, and Britton Chance

***Abstract*—We have developed a flying-spot scanner (FSS), for fluorescence imaging of tissues *in vivo*. The FSS is based on the principles of single-pixel illumination and detection via a raster scanning technique. The principal components of the scanner are a laser light source, a pair of horizontal and vertical scanning mirrors to deflect the laser light in these respective directions on the tissue surface, and a photo multiplier tube (PMT) detector. This paper characterizes the performance of the FSS for fluorescence imaging of tissues *in vivo*. First, a signal-to-noise ratio (SNR) analysis is presented. This is followed by characterization of the experimental SNR, linearity and spatial resolution of the FSS. Finally, the feasibility of tissue fluorescence imaging is demonstrated using an animal model. In summary, the performance of the FSS is comparable to that of fluorescence-imaging systems based on multipixel illumination and detection. The primary advantage of the FSS is the order-of-magnitude reduction in the cost of the light source and detector. However, the primary disadvantage of the FSS its significantly slower frame rate (1 Hz). In applications where high frame rates are not critical, the FSS will represent a low-cost alternative to multichannel fluorescence imaging-systems.**

***Index Terms*—Auto fluorescence, cancer, fluorescence, flying-spot scanner, imaging, *in vivo*, precancer, tissues.**

I. Introduction

FLUORESCENCE spectroscopy is a fast and noninvasive optical method that can probe the biochemical and morphological characteristics of tissue. When tissue is illuminated with specific wavelengths of ultraviolet or visible light (excitation), fluorescent molecules within this medium will absorb the energy and emit it as fluorescent light at longer wavelengths (emission). Fluorophores in tissue include amino acids, structural proteins, enzymes, and co-enzymes, lipids and porphyrins [1]–[3]. Nonfluorescent absorbing (hemoglobin) and scattering (extra-cellular/cellular components) molecules also modulate the tissue fluorescence over this wavelength range [1]–[3].

Steady-state fluorescence spectroscopy has been extensively employed to detect epithelial precancers and cancers from small tissue regions (<a few millimeters in diameter) in a variety of tissue sites, including the colon, cervix, and bronchus [1]–[3]. This technique has a high sensitivity and specificity for discriminating between diseased and nondiseased tissue [3]. Steady-state fluorescence imaging has been utilized to a much lesser extent to detect epithelial precancers and cancers from relatively large tissue fields (>a few centimeters in diameter) within the upper aero-digestive tract, tracheo-bronchial tree, and gastrointestinal tissue [1]–[3]. Specifically, several groups have developed endoscopic-compatible [4]–[10] and nonendoscopic-based [11]–[13] fluorescence-imaging systems for these applications. These systems are based on multipixel illumination and detection. Multipixel illumination requires the use of high-powered light sources to illuminate a large tissue area such that there is sufficient power density/pixel. Multipixel detection is achieved using a charge-coupled device (CCD) camera. The requirement for high-powered light sources and CCD cameras renders these systems expensive.

Our group has developed a flying-spot scanner (FSS), which may reduce the cost associated with previously developed fluorescence-imaging systems. The FSS is based on single-pixel illumination and detection and its principal components are a low-power light source, a pair of horizontal and vertical scanning mirrors to deflect the light in these respective directions on the tissue surface, and a photo multiplier tube (PMT) detector. The FSS is similar in principle to the commercially available scanning laser ophthalmoscope (SLO) [14]. The SLO is an imaging device designed to view the inner parts of the human eye. Its principle is based on the optical scanning of a laser beam and the detection of the reflected light intensity. The SLO obtains fundus information with temporal encoding and forms the images electronically as the beam scans. The SLO realizes high image contrast and low stray light detection with a striking depth of focus due to a confocal optical arrangement. However, the confocal arrangement limits the working distance of the SLO. The FSS, which is nonconfocal provides an adjustable working distance, which is at least a factor of three greater than that of the SLO albeit with less efficient stray light rejection. The FSS represents a novel approach for fluorescence imaging of human epithelial precancers.

The purpose of this report is to characterize the performance of the FSS for fluorescence imaging of tissues, *in vivo*. First, a signal-to-noise ratio (SNR) analysis is presented. This is followed by characterization of the experimental SNR, linearity and spatial resolution of the FSS. Finally, the feasibility of tissue fluorescence imaging is demonstrated using animal models.

Manuscript received September 5, 2000; revised May 20, 2001. This work was supported by the National Institutes of Health (NIH) under Grant: RO1 CA72650. *Asterisk indicates corresponding author.*

*N. Ramanujam is with the Department of Biomedical Engineering, University of Wisconsin, Madison, WI 53706 USA (e-mail: nimmi@engr.wisc.edu).

J. Chen and B. Chance are with the Department of Biochemistry and Biophysics, University of Pennsylvania, Philadelphia, PA 19104 USA.

K. Gossage and R. Richards-Kortum are with the Department of Electrical and Computer Engineering, University of Texas, Austin, TX 78712 USA.

Publisher Item Identifier S 0018-9294(01)07447-X.

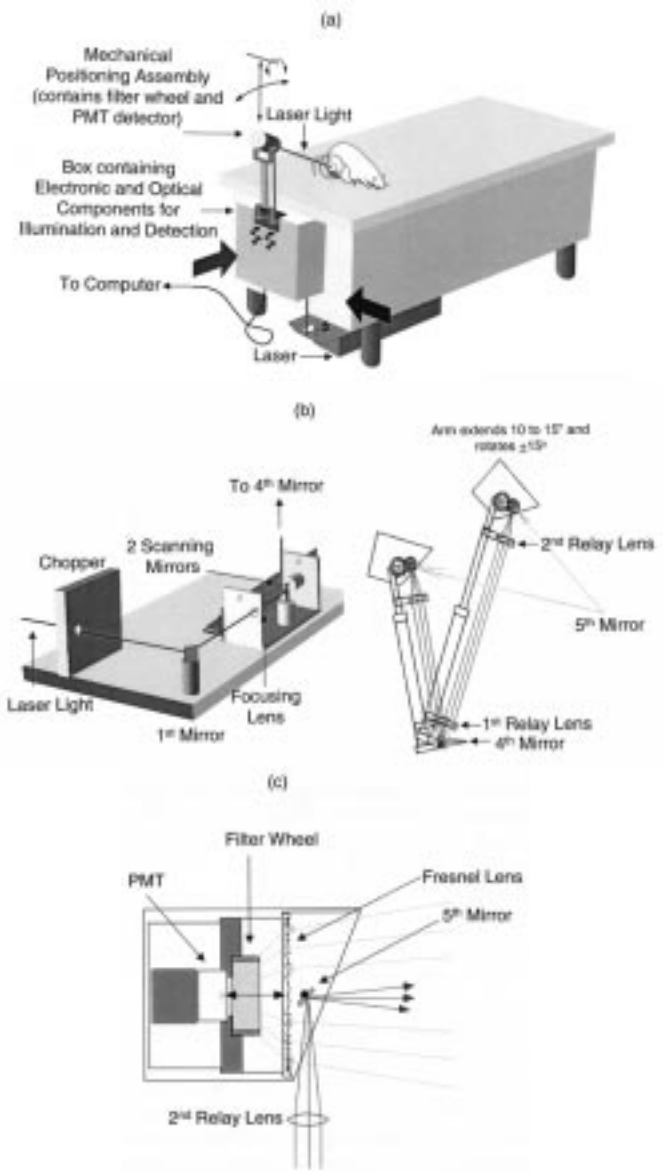

Fig. 1. A detailed schematic of the FSS. (a) Primary components. (b) Optical illumination path. (c) Optical detection path.

II. Methods

A. Description of the FSS

A detailed schematic of the FSS is shown in Fig. 1(a)–(c). The FSS was constructed at the University of Pennsylvania. The scanner consists of three primary components as shown in Fig. 1(a). A 442-nm wavelength, Helium–Cadmium laser (Model 4207-NB, Liconix) is the light source. A mechanical positioning assembly directs the excitation light from the laser to the tissue and directs the emitted light from the tissue though a filter wheel into a PMT (R5600P-01, Hamamatsu). The assembly also provides three degrees of freedom for positioning the PMT: tilt, rotation, and translation. Between the laser and the assembly is a box, which contains the electronic and optical components for deflection of the laser illumination in the horizontal and vertical directions, electronics for signal detection and processing, and a computer interface.

The optical path from the laser to the tissue is shown in Fig. 1(b). The laser light passes through a chopper, two scanning mirrors, and a series of plano convex lenses and flat mirrors, before it is incident on the tissue surface. The chopper has 30 circular apertures and rotates at 256 revolutions/s, thus modulating the laser light at a frequency of 7.68 KHz. The horizontal and vertical scanning mirrors deflect the laser light at a frequency of 120 Hz and 1.875 Hz, respectively. The focusing lens has a focal length of 12.5 cm and a 1 cm diameter. The 1st and 2nd relay lens have a focal length of 7.5 cm and a 5 cm diameter.

The collimated laser light is focused with a lens at a point that is midway between the horizontal and vertical scanning mirrors. It is then re-collimated by the 1st relay lens and re-focused by the 2nd relay lens onto a 5 mm $\times$ 5 mm flat mirror (5th mirror) within the head of the mechanical positioning assembly. The high frequency deflection of the horizontal scanning mirror results in a line image, rather than a point image and the slow deflection of the vertical scanning mirror results in a slow sweep of this image on the 5th mirror. From the 5th mirror, the laser light diverges and impinges onto the tissue surface at a distance of 6 cm (this working distance can be varied). The line image and vertical sweep observed at the 5th mirror is magnified at the tissue surface. The overall magnification of the laser light is determined by the ratio of the distance between the tissue surface and 5th mirror (6 cm) and the focal length of the focusing lens (12.5 cm). The diameter of the laser light (2 mm in diameter) is de-magnified by a factor of two (1 mm in diameter) at the tissue surface. The relay lenses allow for the adjustment of the height of the mechanical positioning assembly, without altering the magnification of the laser light.

The excitation light is scanned across the tissue surface. The emitted light from each discrete pixel (1 mm in diameter) is collected and focused by a Fresnel lens (focal length: 2 cm, diameter: 5 cm) onto the PMT cathode [Fig. 1(c)]. The lens is located within the head of the mechanical positioning assembly at a distance of 8 cm from the tissue surface. Between the Fresnel lens and the PMT is a filter wheel that has 4 slots for 0.5 cm diameter filters. During fluorescence measurements, the fluorescence at 525 nm $\pm$ 25 is detected, while the back-scattered excitation light at 442 nm is rejected. In order to achieve this, two band-pass filters, each with a peak transmission of 50% at 525 nm, a full width half maximum of 50 nm and an O.D of 5.0 at 442 nm are used to selectively transmit the fluorescence. In addition to the fluorescence measurements, reflectance measurements are made at the excitation wavelength of 442 nm. A neutral density filter of optical density (O.D.) 3.0 is used in a second filter wheel slot to ensure that the fluorescence and reflectance signals are within the same dynamic range.

The scanning format of the FSS is shown in Fig. 2. The sampling period/pixel is 130 μs (inverse of the chopper frequency). During this period, both the light and dark interval of the chopped light are sampled equally. Hence, each data point contains a dark and light half-pixel. The time for one horizontal scan is 8.33 ms and a total of 64 data points are obtained. The time for one vertical scan is 0.533 s and 4096 data points are imaged. Two vertical scans (forward and backward) are used to provide a total of 8192 data points. The difference between each light half-pixel and corresponding dark half-pixel for a particular data point is obtained from the forward and backward

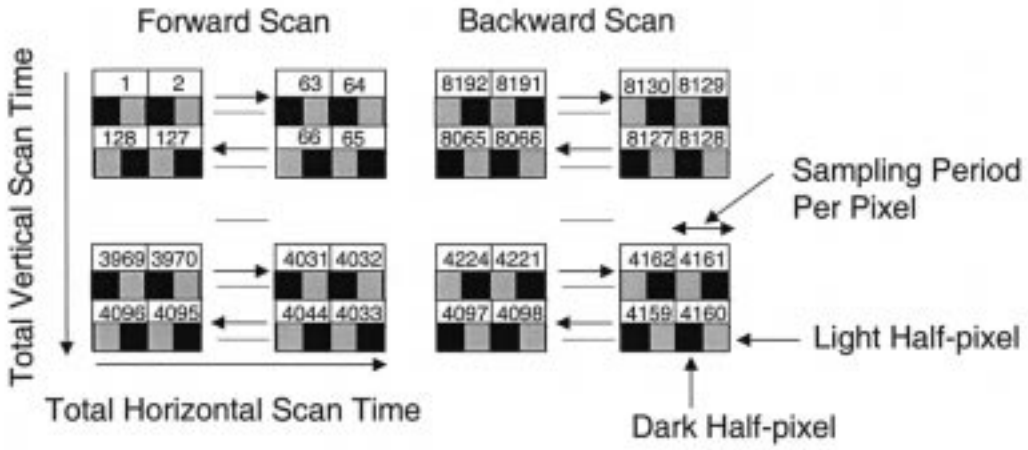

Fig. 2. The scanning format of the FSS. The sampling period/pixel is 130 μs (inverse of the chopper frequency). During this period both the light and dark interval of the chopped light are sampled equally. Hence, each data point contains a dark and light half-pixel. The time for one horizontal scan is 8.33 ms and a total of 64 data points are obtained. The time for one vertical scan is 0.533 s and 4096 data points are imaged. Two vertical scans (forward and backward) are used to provide a total of 8192 data points. The difference between each light half-pixel and corresponding dark half-pixel for a particular data point is obtained from the forward and backward scans (for example, the difference between pixel 1 and 8192). The resulting image contains 4096 data points, where each pixel contains two, light half-pixels corrected for the dark current of the PMT and ambient light.

scans (for example, the difference between pixel 1 and 8192). The resulting image contains 4096 data points, where each pixel contains two, light half-pixels corrected for the dark current of the PMT and ambient light. The FSS, therefore, accounts for ambient light conditions and the dark current through a simple real-time subtraction scheme. When this approach is used, the PMT detects the dark current, ambient light and the tissue fluorescence simultaneously during the light interval and just the dark current and the ambient light during the dark interval. The primary requirement in using this approach is that the ambient light contribution does not use up the dynamic range of the PMT. Several measures were taken to ensure that the ambient light contribution was minimized during operation of the scanner. A band pass filter with a peak transmission at 525 and a 50-nm bandpass (placed directly in front of the PMT) was used to rejected ambient light at wavelengths that were outside of the band pass with an O.D. of ten. Furthermore, incandescent lighting rather than fluorescent lighting was used during operation of the scanner to further reduce the ambient light contribution in the visible spectral region in which tissue fluorescence was measured.

B. SNR Calculation

The expected SNR for tissue fluorescence measurements with the FSS was calculated by estimating losses at three stages; 1) the optical illumination path; 2) the conversion of the excitation light to emitted light; and 3) the optical detection path. Table I indicates all the input parameters for the optical illumination and detection path. Additionally, the calculated parameters required for SNR determination are indicated. The system throughput calculation indicates that the SNR for fluorescence measurements is 65 and it is shot noise limited.

C. Characterization of the FSS

Experiments were performed to characterize the performance of the FSS. Specifically, the SNR, background noise, linearity, and spatial resolution of the scanner were determined.

A 5 $\times$ 5-cm absorption glass filter (OG530, Omega Optics) was used for the SNR measurements. The filter when excited in the blue fluoresces in the green. First, the filter was placed in the object plane of the FSS (6-cm working distance). Then, the high voltage of the PMT was set to be between 525–575 V, which is in the range used for tissue experiments. Then, the laser light was attenuated with a neutral density filter, until the fluorescence detected was in the same range as that from tissues. Nine consecutive frames (one forward scan and one backward scan in each frame) were obtained. The average and the standard deviation were calculated for a 3 $\times$ 3 pixel area at the center of the fluorescence image and the SNR was determined from the ratio of these values. SNR values were calculated for three, six, and nine frames.

Background noise measurements were made from a container of distilled water in a manner similar to that described for the filter. The background includes any nontissue fluorescence and back-scattered excitation light. Distilled water is appropriate for background noise characterization because it does not fluoresce, but has a refractive index that is similar to that of tissue [15]. Therefore, it will reflect the same fraction of the excitation light (specular reflection), as the tissue surface will. However, distilled water unlike tissue, does not diffusely scatter light. Since the collected diffuse reflectance of tissue is expected to be at least an order of magnitude lower than the collected specular reflection, the contribution of this component to the background noise can be ignored. The background noise was averaged from a central, 3 $\times$ 3 pixel area, averaged from three frames.

Linearity measurements were made using the absorption glass filter in a manner similar to that described for the SNR measurements. The laser power was attenuated using neutral density filters, with an O.D. range of 0.03–1.8. The measured attenuation in fluorescence was calculated in units of O.D. and averaged from a central, 3 $\times$ 3 pixel area, which was averaged from three frames and compared to the attenuation of the neutral density filter used.

TABLE I
THE INPUT PARAMETERS AND THE CALCULATED PARAMETERS REQUIRED FOR DETERMINING THE SIGNAL TO NOISE RATIO OF THE FSS

Optical Illumination	**Symbol**	**Quantity**
Laser power (mW)	P_o	15
Transmission through chopper	T_c	.9
Reflective efficiency of 1st mirror	R_{M1}	0.7
Transmission through focusing lens	T_{L1}	0.96
Fresnel reflection losses through focusing lens	R_{L1}	0.08
Reflective efficiency of the two scanning mirrors	R_{SM}	0.49
Reflective efficiency of 4th mirror	R_{M4}	0.7
Transmission through 1st relay lens	T_{RL1}	0.96
Fresnel reflection losses through 1st relay lens	R_{RL1}	0.08
Transmission through 2nd relay lens	T_{RL2}	0.96
Fresnel reflection losses through 2nd relay lens	R_{RL2}	0.08
Reflective efficiency of 5th mirror	R_{M5}	0.7
Ratio of emitted and excitation light	**Symbol**	**Quantity**
Tissue fluorescence efficiency (approximate) (442 nm excitation, 525 nm emission)	FE [4]	~1E-05
Optical Detection	**Symbol**	**Quantity**
Integration time (s)	ΔT	1.3e-06
Distance between tissue and Fresnel lens (cm)	D	8
Radius of Fresnel lens (cm)	R	2.5
Transmission through Fresnel lens	T_{FR}	0.96
Fresnel reflection losses through Fresnel lens	R_{FR}	0.08
Transmission through band pass filter	T_{BP}	0.25
Plancks constant (J.s)	H	6.626E-34
Speed of light (m/s)	C	2.9979E+08
Peak emission wavelength (nm)	λ	525
Quantum efficiency	QE	0.15
Dark charge (e^-/s)	DC	50
Calculated Parameters	**Symbol and Calculation**	**Quantity**
Effective transmission in the illumination path	$T_I = T_c \times R_{M1} \times T_{L1} \times (1-R_{L1}) \times R_{SM} \times R_{M4} \times T_{RL1} \times (1-R_{RL1}) \times T_{RL2} \times (1-R_{RL2}) \times R_{M5}$	0.105
Illuminated power (W)	$P_I = T_I \times P_o$	1.57E-03
Emitted power (W)	$P_E = FE \times P_I$	1.57E-08
Emitted energy (J)	$E_E = P_E \times \Delta T$	2.04E-12
Collection efficiency	$CE = \pi r^2/4\pi D^2$ [4]	0.0233
Effective transmission in the detection path	$T_D = T_{FR} \times (1-R_{FR}) \times T_{BP}$	0.22
Detected energy (J)	$E_D = E_E \times CE \times T_D$	1.05E-14
Detected photons	$P_D = \lambda \times E_D / H \times C$	27826
Photoelectrons	$PE_D = P_D \times QE$	4174
Noise (shot)	$N_S = (PE_D)^{1/2}$	65
Noise (dark current)	$N_D = DC \times \Delta T$	0.0065
Signal to noise ratio	$SNR = PE_D / (N_S + N_D)$	65

The fluorescence image from a resolution target (a piece of black paper with a specific number of white lines/mm printed on it) was recorded in a manner similar to that described for the filter. The maximum number of bars/millimeter in which individual elements could be distinguished was noted from a fluorescence image that was averaged from three frames. The spatial resolution was calculated to be the inverse of this value.

D. Animal Models

Fluorescence and reflectance imaging of tissues, *in vivo* was carried out using an animal model. At 442-nm excitation and 525-nm emission, the fluorescence of tissues is attributed to flavoprotein, which is an electron carrier in the metabolic pathway in cells [16]. The fluorescence of flavoprotein is maximal when it is oxidized and minimal when it is reduced [16]. Furthermore, the reabsorption effects of hemoglobin also attenuate the fluorescence at the excitation and emission wavelengths [17]. Oxygenated hemoglobin has a lower absorption coefficient than deoxygenated hemoglobin at 442-nm excitation. At emission wavelengths between 500 and 550 nm, the absorption of both are similar [17].

Three sets of experiments were carried out in which perturbations of flavoprotein fluorescence and/or hemoglobin absorption were induced. First, global perturbations in the rat brain were induced, by lowering the fraction of inspired oxygen (FiO_2). In the second experiment, a local injury was induced in the rat brain, by the subdural insertion of a fine, 26-gauge needle. Finally, 9L glioma tumor cells were injected into the rat flank and allowed to grow for one to two weeks to produce palpable tumors. In the first two studies, fluorescence images that were acquired after the perturbation were normalized to that

which, were acquired before the perturbation to account for the nonuniform excitation and emission geometry. No reflectance images were acquired in these studies. In the tumor studies, fluorescence and reflectance images were acquired from the tumor and adjacent muscle tissue sites. The fluorescence image was normalized to the reflectance image to account for geometrical artifacts.

Male Fischer 344 rats (Harlan Sprague Dawley Inc., Indianapolis, IN) weighing between 100–150 g were used. These rats were housed with *ad libitum* access to food and water, and kept under controlled conditions (22 °C, relative humidity 45%–55%, 12 hour light/dark cycle). Animal care and procedures were in accordance with the guidelines in the U.S. department of Health and Human Services and National Institutes of Health "Guide for the Care and Use of Laboratory Animals" and was approved by the Institutional Animal Care and Use Committee.

1) Fluorescence Imaging of the Exposed Rat Brain During Global and Local Perturbations: Each rat was anesthetized by intraperitoneal injection of Nembutal (30–35 mg/kg). A craniotomy was performed to expose an area of the brain (parietal region) that was approximately 1 cm^2. In the global perturbation protocol, a gas mask, which was connected to nitrogen (N_2) and oxygen (O_2) tanks via flow meters was placed over the animal's nose and mouth. The exposed brain was then placed at the object plane of the FSS. First, the animal was allowed to inhale 21% O_2 (total volume: 1 liter). Subsequently, the FiO_2 was lowered such that the animal underwent a transition from a normoxic (21% O_2) to hypoxic (5% O_2) to in some cases, anoxic state (100% N_2). In the local perturbation experiment, instead of lowering the FiO_2 to the animal, a fine, 26-gauge, needle was inserted subdurally into the exposed brain.

2) Fluorescence and Reflectance Imaging of the 9L Glioma Tumor on the Rat Flank: Cells derived from the 9L rat glioma tumor were used to develop subcutaneous tumors in the rat. Each rat was anesthetized and injected with 1×10^6 tumor cells (0.1-ml suspension) subcutaneously in the flank. The tumor was allowed to grow for one to two weeks until its size was approximately 1 cm in diameter. Then, the animal was anesthetized, the skin was peeled off the tumor and the exposed area was placed in the object plane of the FSS. Fluorescence and reflectance images were acquired from the tumor and the adjacent muscle site in a serial manner.

III. Results

A. Characterization of FSS

The experimental SNR, background noise, linearity, and spatial resolution of the scanner were determined as described previously. The average experimental SNR was estimated to be 25 $\pm$10 from three frames. It was 25 $\pm$7 when six frames were averaged and increased to 27 $\pm$6 when nine frames were averaged. The calculated SNR/pixel was estimated to be 65. The experimental SNR is within a factor of two of the calculated SNR. The average background noise was 0.0186 V and this was less than 1% of the fluorescence intensity measured from tissue. The linearity test of the FSS indicated that there is a one-to-one correspondence between the measured and expected O.D. over a range of at least two O.D. (correlation coefficient = 0.9926). The slope of the best fit between the two parameters was 0.98. Finally, the maximum number of resolvable bars/millimeter of the resolution target was one. Therefore, the resolution was determined to be 1 mm. The resolution target was also used to calibrate the scale of the tissue fluorescence images.

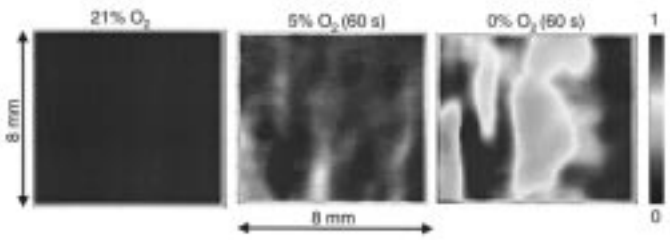

Fig. 3. Fluorescence images acquired from the exposed rat brain during different FiO_2 levels. Each image has been divided by a base line image that was obtained when the rat underwent 21% O_2 inhalation.

B. Animal Model Studies

Fig. 3 displays fluorescence images acquired from the exposed rat brain during different FiO_2 levels. Each image has been divided by a base line image that was obtained when the rat underwent 21% O_2 inhalation. Hence, the first normalized image has a uniform intensity of one. When the animal undergoes 5% O_2 inhalation, there is a 20%–30% decrease in the intensity. When the animal undergoes 100% N_2 inhalation, there is more than a 50% decrease in intensity in some parts of the brain. Note that the decrease in fluorescence intensity will be somewhat enhanced by the effect of deoxygenated hemoglobin absorption, which is greater than that of oxygenated hemoglobin absorption. These images provide the dynamic range for fluorescence measurements at 442-nm excitation and 525-nm emission from living tissue.

Fig. 4 shows a line plot of the mean fluorescence intensity measured from the exposed rat brain during an inhalation protocol in which the animal underwent a transition from 21% O_2 to 5% O_2 inhalation for a period of 2 min, and then back to 21% O_2 inhalation. Each data point corresponds to the intensity averaged from one image. Cycles 1 and 2 represent data from two consecutive experiments. The plot corresponding to cycle 1 indicates that when the animal makes a transition from 21% to 5% O_2 inhalation, there is a 15% decrease in the mean intensity, which reverts back to the base line when the animal inhales 21% O_2. This is reproduced in cycle 2, thus, demonstrating the reproducibility of fluorescence imaging from living tissue.

Fig. 5 displays normalized fluorescence images from the exposed rat brain before and after subdural insertion of a fine, 26-gauge, needle. Measurements were made over a 45-min period, after the perturbation was induced. The normalized image right after the perturbation (6 s) indicates that there is a local region (1–2 mm) of decreased intensity that increases in area as a function of time. After 8 min, the local area of decreased intensity regresses, ultimately reverting back close to the base line at 45 min.

Fig. 6 displays 1) fluorescence and reflectance ratio (F/R) images; 2) normalized F/R profiles of the 9L glioma tumor (nine-days old) and adjacent muscle tissue in the rat flank. In

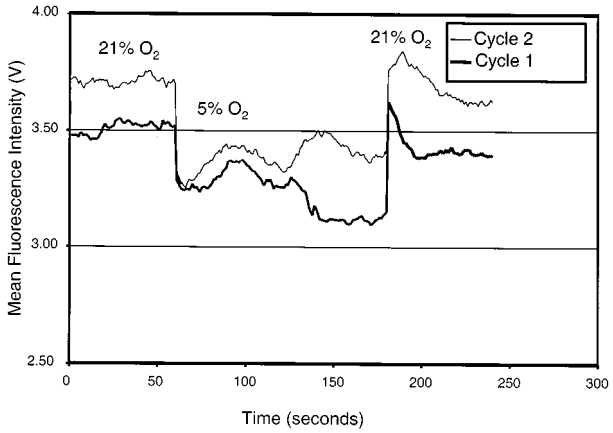

Fig. 4. A line plot of the mean fluorescence intensity measured from the exposed rat brain during an inhalation protocol in which the animal underwent a transition from 21% O_2 to 5% O_2 inhalation for a period of 2 min, and then back to 21% O_2 inhalation. Each data point corresponds to the mean intensity averaged from one image. Cycles 1 and 2 represent data obtained from two consecutive experiments.

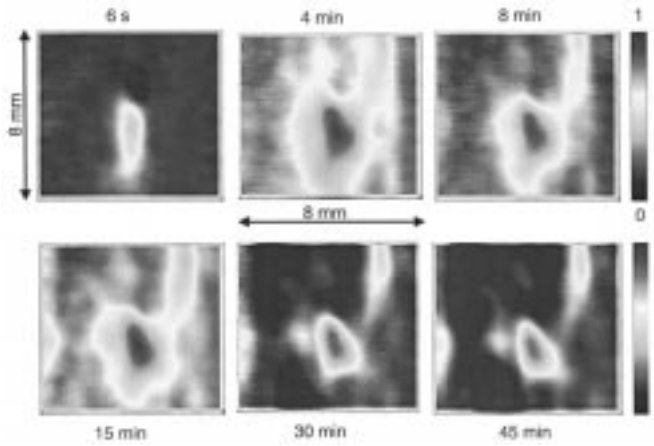

Fig. 5. Normalized fluorescence images from the exposed rat brain before and after subdural insertion of a fine, 26-gauge, needle. Measurements were made over a 45-min period, after the perturbation was induced.

Fig. 6(a), the delineation between the tumor and muscle tissue (black contour) was corroborated by visual observation of the two regions. The tumor F/R ranges from 2–4, while that of the muscle ranges from 0–2. The normalized F/R profile through several cross-sections of the tumor and adjacent muscle in Fig. 6(a) are shown in Fig. 6(b). The F/R profiles have been normalized to a maximum intensity of one. The F/R of the tumor is as much as a factor of five higher than that of the adjacent muscle. This suggests that there is either an increase in the fluorescence and/or a decrease in the reflectance of the tumor relative to that of muscle tissue.

Fig. 7 displays a bar chart of the ratio of F/R of the tumor to F/R of adjacent muscle tissue, in a total of nine rats. The highest F/R in the tumor region was divided by the lowest F/R in the muscle tissue. The ratio ranges from 0.2–6. Half of the tumors have an F/R that is greater than that of muscle tissue. The other half shows the opposite result. The tumors that have an increased F/R are 7–9 days old, while those with a decreased F/R are more than ten days old.

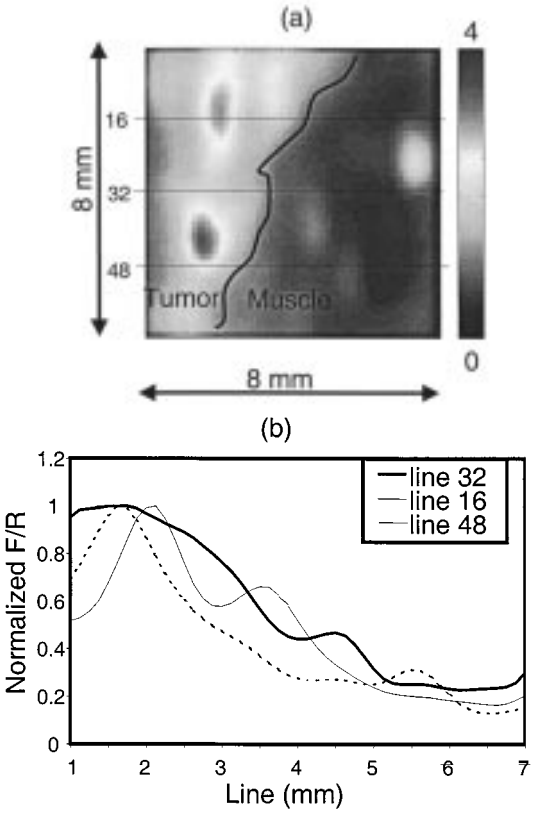

Fig. 6. (a) F/R images and (b) normalized F/R profiles of the 9L glioma tumor (nine days) and adjacent muscle tissue in the rat flank.

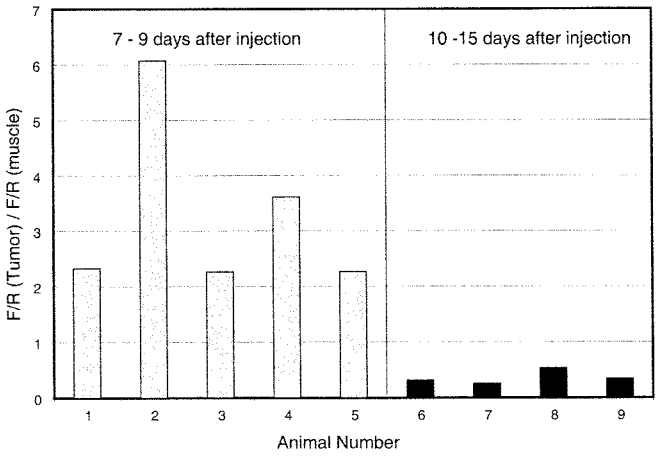

Fig. 7. Bar chart displaying the ratio of the following two parameters: the F/R of the tumor and F/R of adjacent muscle tissue, in a total of nine rats. Specifically, the highest F/R in the tumor region was divided by the lowest F/R in the adjacent, muscle tissue region.

IV. Discussion and Conclusion

The FSS provides fast and noninvasive fluorescence imaging of living tissues. Our goal is to use the scanner to image the fluorescence intensity at several excitation-emission wavelength pairs from normal and precancerous tissues of the human cervix. The SNR, dynamic range and spatial resolution of the FSS are adequate for the proposed application. The SNR, which is approximately 30 : 1 is greater than the SNR requirement

of 25 : 1 reported by Utzinger *et al.* [18] for discriminating between normal tissues, low-grade and high-grade precancers of the cervix. Furthermore, since the fluorescence efficiency of normal tissues, low-grade and high-grade precancers are within a factor of two of each other [19], the dynamic range of the FSS, which is at least two O.D., is sufficient for fluorescence imaging of cervical tissues. Finally, the FSS was designed to achieve a spatial resolution of approximately 1 mm. This is based on the fact that biopsies of suspicious lesions from the cervix taken during a conventional diagnostic procedure are typically between 1–8 mm^3. Note that the resolution target does overestimate the spatial resolution of the FSS for tissue fluorescence imaging. The spatial resolution in tissue is expected to degrade slightly due to the multiple scattering of light in this medium.

The fluorescence images obtained from the animal model experiments were normalized in order to compensate for geometrical effects of the excitation and emission geometry. In the case of 9L glioma tumor, the fluorescence image was divided by the corresponding reflectance image. Qu *et al.* [20] have reported the use of F/R imaging to correct geometrical artifacts during fluorescence imaging of tissue phantoms. They were able to correct their fluorescence images more effectively by normalizing them to the diffuse reflection image rather than to the total reflection image (diffuse and specular reflection). They concluded that the specular reflection causes major artifacts by saturating a large area of the CCD detector. In our experiments, the total reflection measurements from the 9L glioma tumor were kept within the linear range of the PMT. Therefore, we do not expect artifacts from detector saturation to affect these images. However, in future studies we will explore the use of cross-polarization imaging to reject the specular component from our reflectance images.

The FSS represents a significant decrease in cost, relative to multichannel, fluorescence-imaging systems. The reduction in cost would result from the use of relatively low-power light sources and single-channel detectors. However, it is important to confirm that the less-expensive FSS performs comparably to the multichannel systems. To address this issue, we compared the performance of the FSS to a multichannel fluorescence-imaging system developed by Wang *et al.* for the detection of precancers in the colon [4]. Their system consists of a high-powered Argon laser and an intensified charge-injection device camera. The characteristics of the two systems are shown in Table II. The multichannel system illuminates a 40 mm diameter area with a power density of 0.239 mW/mm^2. If the illumination area is reduced to 10 mm in diameter, the power density is increased to 4 mW/mm^2, which is within a factor of two reported for the FSS. A reduction in the working distance by a factor of two doubles the spatial resolution of the FSS, making both the working distance and spatial resolution of the single-channel system comparable with that of the multichannel system. The SNR of the two systems are also very similar. However, the frame rate of the multichannel system is 30 times faster compared to that of the FSS. Thus, it can be concluded that the FSS will represent a low-cost alternative to multichannel fluorescence imaging-systems in applications where high frame rates are not required.

TABLE II
A COMPARISON OF THE CHARACTERISTICS OF THE SINGLE-CHANNEL FSS TO A MULTICHANNEL FLUORESCENCE-IMAGING SYSTEM DEVELOPED BY WANG *et al.*

Parameters	Single-Channel System	Multi-Channel System
Power (mW)	15	300
Diameter of illuminated area (mm)	10	40
Power density (mW/mm^2)	2	0.239
Working distance (mm)	60	20
Spatial resolution measured using similar resolution targets (mm)	1.0	0.5
Signal-to-noise (3 x 3 pixel area averaged from 6 frames)	25±7	32±5
Frame rate (s)	1	0.033 s

The animal model studies performed with the FSS indicated several interesting findings that are discussed below. In the global perturbation protocol, oscillations in the mean fluorescence are observed from the rat brain when the FiO_2 is decreased from 21% to 5% O_2 (Fig. 4). The oscillation disappears when the FiO_2 is increased back to 21%. Dora *et al.* [21] have observed similar oscillations in the fluorescence of pyridine nucleotides from the exposed rat brain during a transition from normoxia (30% O_2) to hypoxia (6% O_2). They attribute the oscillations during hypoxia to metabolism-related changes in the contraction of the heart.

In the local perturbation experiment, the propagation of a local area of decreased fluorescence intensity can be attributed to a metabolic insult and/or a microscopic bleed (no visible bleeding was observed at the end of the experiment). However, because reflectance images were not obtained in these experiments, it is difficult to delineate between the effects of bleeding versus metabolic change. However, regression of the local area of decreased intensity after a 45-min period suggests that the subdural perturbation may have resulted in a temporary metabolic insult rather than the extravasation of blood due to capillary injury.

F/R images acquired from the 9L glioma tumor on the rat flank suggest that the metabolic and/or vascular state of the tumor appear to correlate well with the age and, hence, the size of the tumor [22]. However, it is not clear what the basis is for the sharp transition between the F/R ratios of the two different tumor age groups in our studies. More fluorescence studies with corresponding histopathology of the both the visually appearing tumor region and adjacent muscle tissue are required to confirm these preliminary findings.

ACKNOWLEDGMENT

The authors would like to thank T. Jenkins of the Department of Radiation Oncology, University of Pennsylvania, for providing the 9L glioma cells.

REFERENCES

[1] G. A. Wagnieres, W. M. Star, and B.C. Wilson, "*In vivo* fluorescence spectroscopy and imaging for oncological applications," *Photochem. Photobiol.*, vol. 68, no. 5, pp. 603–632, 1998.

[2] R. Richards-Kortum and E. Sevick-Muraca, "Quantitative optical spectroscopy for tissue diagnosis," *Annu. Rev. Phys. Chem.*, vol. 47, pp. 555–606, 1996.

[3] N. Ramanujam, "Fluorescence spectroscopy of neoplastic and nonneoplastic tissues," *Neoplasia*, vol. 2, no. 1, pp. 1–29, 2000.
[4] T. D. Wang, J. M. Crawford, M. S. Feld, Y. Wang, I. Itzkan, and J. Van Dam, "*In vivo* identification of colonic dysplasia using fluorescence endoscopic imaging," *Gastrointest. Endosc.*, pt. 1, vol. 49, no. 4, pp. 447–455, 1999.
[5] C. S. Betz, M. Mehlmann, K. Rick, H. Stepp, G. Grevers, R. Baumgartner, and A. Leunig, "Autofluorescence imaging and spectroscopy of normal and malignant mucosa in patients with head and neck cancer," *Lasers Surg. Med.*, vol. 25, pp. 323–334, 1999.
[6] B. Palcic, S. Lam, and J. Hung *et al.*, "Detection and localization of early lung cancer by imaging techniques," *Chest*, vol. 99, pp. 742–743, 1991.
[7] P. S. Anderson, S. Montan, T. Persson T, S. Svanberg, S. Tapper, and S.-E. Karlsson, "Fluorescence endoscopy instrumentation for improved tissue characterization," *Med. Phys.*, vol. 14, no. 4, pp. 633–636, 1987.
[8] G. A. Wagnieres, A. P. Studzinski, and H. E. van den Bergh, "An endoscopic fluorescence imaging system for simultaneous visual examination and photodetection of cancers," *Rev. Sci. Instr.*, pt. 1, vol. 68, no. 1, pp. 203–212, 1997.
[9] T. Mckechnie, A. Jahan, I. Tait, A. Cuschieri, W. Sibbett, and M. Padgett, "An endoscopic system for the early detection of cancers of the gastrointestinal tract," *Rev. Sci. Instr.*, vol. 69, no. 6, pp. 2521–2523, 1998.
[10] H. Zeng, A. Weiss, R. Cline, and C. E. MacAulay, "Real-time endoscopic imaging for early cancer detection in the gastrointestinal tract," *Bioimaging*, vol. 6, no. 4, pp. 151–165, 1998.
[11] B. W. Chwirot, S. Chwirot, J. Redzinski, and Z. Michiniewicz, "Detection of melanomas by digital imaging of spectrally resolved ultraviolet light induced autofluorescence of human," *Eur. J. Cancer*, vol. 34, no. 11, pp. 1730–1734, 1998.
[12] P. S. Andersson, S. Montan, and S. Svanberg, "Multispectral system for medical fluorescence imaging," *IEEE J. Quantum Electron.*, vol. QE-23, pp. 1798–1805, Oct. 1987.
[13] S. Andersson-Engels, J. Johansson, and S. Svanberg, "Medical diagnostic system based on simultaneous multispectral fluorescence imaging," *Appl. Opt.*, vol. 34, no. 1, pp. 8022–8029, 1994.
[14] R. H. Webb, G. W. Hughes, and F. C. Delori, "Confocal laser scanning ophtalmoscope," *Appl. Opt.*, vol. 26, pp. 1492–1499, 1987.
[15] S. L. Jacques, "Monte-Carlo methods," in *Optical-Thermal Response of Laser-Irradiated Tissue*, A. J. Welch and M. J. C. van Gemert, Eds. New York: Plenum, 1995, pp. 73–99.
[16] B. Chance, B. Schoener, R. Oshino, F. Itshak, and Y. Nakase, "Oxidation-reduction ratio studies of mitochondria in freeze-trapped samples," *J. Biol. Chem.*, vol. 254, no. 11, pp. 4764–4771, 1979.
[17] S. B. Brown, *An Introduction to Spectroscopy for Biochemists*. London, U.K.: Academic, 1980.
[18] U. Utzinger, E. V. Trujillo, E. N. Atkinson, M. F. Mitchell, S. B. Cantor, and R. Richards-Kortum, "Performance estimation of diagnostic tests for cervical precancer based on fluorescence spectroscopy: Effects of tissue type, sample size, population and signal-to-noise ratio," *IEEE Trans. Biomed. Eng.*, vol. 46, pp. 1293–1303, Nov. 1999.
[19] E. V. Trujillo, D. R. Sandison, U. Utzinger, N. Ramanujam, M. Follen Mitchell, and R. Richards-Kortum, "Method to determine tissue fluorescence efficiency *in vivo* and predict signal-to-noise ratio for spectrometers," *Appl. Spec.*, vol. 52, no. 7, pp. 943–951, 1998.
[20] J. Y. Qu, Z. Huang, and J. Hua, "Excitation-and-collection geometry insensitive fluorescence imaging of tissue-simulating turbid media," *Appl. Opt.*, vol. 39, no. 19, pp. 3344–3356, 2000.
[21] S. E. Dora, K. Olaffson, B. Chance, and A. G. B. Kovach, "Monte-Carlo methods," in *Oxygen Transport to Tissue—II*, J. Grote, D. Reneau, and G. Thews, Eds. New York: Plenum, 1976, pp. 299–305.
[22] E. K. Rofstad, B. M. Fenton, and R. M. Sutherland, "Intracapillary HbO_2 saturations in murine tumors and human tumor xenografts by cryospectrophotometry: Relationship between tumor volume, tumor pH and fraction of radiobiologically hypoxic cells," *Br. J. Cancer.*, vol. 57, no. 5, pp. 494–502, 1988.

Nirmala Ramanujam received the B.S. degree in mechanical engineering from the University of Texas at Austin in 1989. She received the M.S. degree in mechanical engineering and Ph.D. degree in biomedical engineering, in 1992 and 1995, respectively, also from the University of Texas.

In 1996, she joined the Biochemistry and Biophysics Department at the University of Pennsylvania, University Park, as a Post-doctoral Fellow.Currently, she is an Assistant Professor in the Department of Biomedical Engineering at the University of Wisconsin, Madison. Her research focuses on the application of optical spectroscopy for characterization and detection of disease processes in tissue. Her current projects include noninvasive characterization of biological tissues using ultraviolet-visible fluorescence spectroscopy, and photon migration techniques.

Dr. Ramanujam received the National Institutes of Health post-doctoral fellowship in 1997 for research on tissue optical spectroscopy.

JinXian Chen, photograph and biography not available at time of publication.

Kirk Gossage, photograph and biography not available at time of publication.

Rebecca Richards-Kortum received the B.S. degree in physics and mathematics with highest distinction from the University of Nebraska, Lincoln, in 1985. She received the M.S. and Ph.D. degrees in medical physics from the Massachusetts Institute of Technology, Cambridge, in 1987 and 1990.

In 1990, she joined the faculty of the Department of Electrical and Computer Engineering and the Biomedical Engineering Program at the University of Texas at Austin. Her research focuses on the application of optical spectroscopy and imaging for detection of precancer.

Dr. Richards-Kortum is the 1992 recipient of the Presidential Faculty Fellow Award from the National Science Foundation for excellence in research and teaching. In 2000, she was elected to the Academy of Distinguished Teachers at the University of Texas at Austin.

Britton Chance, photograph and biography not available at time of publication.